Check for updates

THE AMERICAN SOCIETY OF MECHANICAL ENGINEERS
345 E. 47th St., New York, N.Y. 10017

98-GT-82

The Society shall not be responsible for statements or opinions advanced in papers or discussion at meetings of the Society or of its Divisions or Sections, or printed in its publications. Discussion is printed only if the paper is published in an ASME Journal. Authorization to photocopy for internal or personal use is granted to libraries and other users registered with the Copyright Clearance Center (CCC) provided $3/article or $4/page is paid to CCC, 222 Rosewood Dr., Danvers, MA 01923. Requests for special permission or bulk reproduction should be addressed to the ASME Technical Publishing Department.

Copyright © 1998 by ASME All Rights Reserved Printed in U.S.A.

PHYSICS OF AIRFOIL CLOCKING IN A HIGH-SPEED AXIAL COMPRESSOR

Daniel J. Dorney
GMI Engineering & Management Institute
Flint, MI

Om P. Sharma
Pratt & Whitney
East Hartford, CT

Karen L. Gundy-Burlet
NASA Ames Research Center
Moffett Field, CA

ABSTRACT

Axial compressors have inherently unsteady flow fields because of relative motion between rotor and stator airfoils. This relative motion leads to viscous and inviscid (potential) interactions between blade rows. As the number of stages increases in a turbomachine, the buildup of convected wakes can lead to progressively more complex wake/wake and wake/airfoil interactions. Variations in the relative circumferential positions of stators or rotors can change these interactions, leading to different unsteady forcing functions on airfoils and different compressor efficiencies. In addition, as the Mach number increases the interaction between blade rows can be intensified due to potential effects. In the current study an unsteady, quasi-three-dimensional Navier-Stokes analysis has been used to investigate the unsteady aerodynamics of stator clocking in a 1-1/2 stage compressor, typical of back stages used in high-pressure compressors of advanced commercial jet engines. The effects of turbulence have been modeled with both algebraic and two-equation models. The results presented include steady and unsteady surface pressures, efficiencies, boundary layer quantities and turbulence quantities.

The main contribution of the current work has been to show that airfoil clocking can produce significant performance variations at the Mach numbers associated with an engine operating environment. In addition, the growth of turbulence has been quantified to aid in the development of models for the multistage steady analyses used in design systems.

NOMENCLATURE

$\tilde{C}_p$	Pressure amplitude coefficient
P	Pressure
P_t	Total Pressure
S	Entropy, arc-length distance
Tu	Turbulence intensity
U_m	Rotor mean wheel velocity
η	Efficiency
ρ	Density
ω	Loss coefficient, $\Delta P_t / P_{t1}$

SUBSCRIPTS

1	Inlet
4	Exit

INTRODUCTION

The operating environment in a multistage turbomachine is inherently unsteady, with interactions occurring between rotor and stator airfoils. These interactions are both viscous and inviscid in nature. The potential field of each airfoil is inviscid in nature, and mainly affects adjacent airfoil rows. The viscous field is much more complex, with wakes from upstream airfoils convecting many chords downstream and interacting with airfoils and other wakes.

The effects of airfoil clocking (or indexing) on turbine performance have been investigated by Huber *et al.* (1995), Griffin *et al.* (1995) and Dorney and Sharma (1996). The studies showed changes in efficiency on the order of 0.5% as the stators were clocked. The highest efficiencies occurred when the first-stage stator wake impinged on the second-stage stator while the lowest were observed when the first-stage stator wake convected through the middle of the second-stage stator passage.

The effects of airfoil clocking on compressor performance have also received attention during the last few years. One of the first studies of airfoil clocking was performed by Capece (1987),

Presented at the International Gas Turbine & Aeroengine Congress & Exhibition
Stockholm, Sweden — June 2–June 5, 1998

Downloaded from http://asmedigitalcollection.asme.org/GT/proceedings-pdf/GT1998/78620/V001T01A024/2410237/v001t01a024-98-gt-082.pdf by guest on 16 August 2022

who showed the potential performance benefits. Saren *et al.* (1994,1995,1997) have used theoretical, computational and experimental techniques to show that airfoil clocking can be used to increase performance and reduce unsteady aerodynamic loads on airfoils. Hsu and Wo (1997) experimentally demonstrated that rotor clocking can be used to reduce the unsteady loads experienced by downstream blade rows, while in another experimental investigation Walker *et al.* (1997) studied the effects of inlet guide vane clocking on the boundary layer quantities and losses of a downstream stator blade row. Barankiewicz and Hathaway (1997) also performed stator clocking experiments, but their data showed only a 0.2% performance change due to clocking. Gundy-Burlet and Dorney (1997a, 1997b) performed computational studies of stator clocking in a 2-1/2 stage compressor, with the results showing efficiency variations on the order of 0.5-0.8%.

The studies discussed above concluded that the performance benefits obtained through airfoil clocking are the result of both changes in the wake interactions and modifications to the unsteady potential field. However, other than the work of Saren *et al.* (1997), all the studies of airfoil clocking discussed above were performed for low-speed machines.

The purpose of the current investigation has been three-fold:

- Gain a better understanding of the physical processes causing the performance variations when compressor airfoils are clocked
- Verify the performance benefits of airfoil clocking at the Mach numbers associated with an engine operating environment
- Study the growth of turbulence for the purpose of developing models for use in steady multi-stage solution techniques

This study was performed using an unsteady, quasi-three-dimensional Navier-Stokes analysis in which the relative motion between rotors and stators is made possible by the use of a system of patched and overlaid grids. The effects of turbulence are modeled with both algebraic and two-equation models. Results include surface pressures, efficiencies, boundary layer quantities and turbulence quantities.

ALGORITHM

The current work is based on an extension of an approach developed by Rai (1987). The approach is reviewed in brief here. The flow field is divided into two types of zones. O-type grids are used to resolve the flow field near the airfoils. The O-grids are overlaid on H-grids which are used to resolve the flow field in the passages between airfoils. The H-grids are allowed to slip relative to one another to simulate the relative motion between rotors and stators. The thin-layer or full Navier-Stokes equations are solved on both the O- and H-grids. The governing equations are cast in the strong conservation form. A fully implicit, finite-difference method is used to advance the solution of the governing equations in time. A Newton-Raphson subiteration scheme is used to reduce the linearization and factorization errors at each time step. The convective terms are evaluated using a third-order accurate upwind-biased Roe scheme. The viscous terms are evaluated using second-order accurate central differences and the scheme is second-order accurate in time. Details of the solution procedure and boundary conditions are discussed in Dorney and Verdon (1994).

TURBULENCE MODELS

Two models were used to simulate the effects of turbulence. The first model is a two-layer algebraic turbulence model based on the work of Baldwin and Lomax (B-L) (1978). The second model is a two-equation $k-\epsilon$ turbulence model based upon the work of Towne *et al.* (1993). In the current implementation, the equations for the turbulence kinetic energy and dissipation rate are decoupled from the flow equations and solved using an alternating-direction implicit integration scheme. Since Newton-Raphson subiterations are used at each global time step of the flow solver, decoupling the $k-\epsilon$ equations from the flow solver should not affect the time accuracy of the analysis. The convective fluxes in the turbulence equations were discretized using first-order accurate upwind differences, while the dissipation terms were discretized using second-order accurate central differences. The $k-\epsilon$ subroutines were constructed in a modular manner to allow the use of different low Reynolds number approximations; the Chien (1982) low Reynolds number model has been used in the current investigation.

Note, the $k-\epsilon$ equations are solved on both the O- and H-grids, while the B-L model is solved only on the O-grids.

GEOMETRY AND GRID

The $1\frac{1}{2}$-stage compressor geometry used in this study models the midspan sections of the back stages in a typical modern high-pressure compressor. The actual compressor geometry has 116 first-stage stators, 90 rotors and 124 second-stage stators. A dimensionally accurate simulation of this geometry would require the modelling of 58 first-stage stators, 45 rotors and 62 second-stage stators. Simulations using this blade count ratio are not feasible for parametric studies. In the current work, it was decided to assume an equal number of blades (90) in each blade row. The first-stage stators were rescaled by a factor of 116/90 and the second-stage stators were rescaled by a factor of 124/90 in order to maintain the same blockage as in the test article. The rationale behind using equal blade counts in all rows is to highlight the physics of airfoil clocking. Note, modifying the stator blade counts in itself represents a form of airfoil clocking because the locations of the first-stage stator wakes will be modified with respect to the second-stage stator.

The axial gap between the first-stage stator and the rotor is approximately 44% of the rotor axial chord. The axial gap between the rotor and the second-stage stator is approximately 47% of the rotor axial chord. The effects of airfoil clocking were modelled by performing simulations with the second-stage stator located in 8 different (equidistant) locations over one pitch (see Fig. 1).

An O-H zonal grid system is used to discretize the flow field within the compressor. The O-grids for the three blade rows each

Downloaded from http://asmedigitalcollection.asme.org/GT/proceedings-pdf/GT1998/78620/V001T01A024/2410237/v001t01a024-98-gt-082.pdf by guest on 16 August 2022

contained 251 × 51 (streamwise×tangential) grid points. The H-grid for the first-stage stator passage contained 108 × 96 grid points, the H-grid for the rotor passage contained 110 × 96 grid points and the H-grid used to discretize the second-stage stator passage contained 145 × 96 grid points. Thus, the complete grid system for the compressor contained 73,251 grid points. The average value of y^+, the non-dimensional distance of the first grid point above the surface, was approximately 0.75 for all three blade rows. In addition, the boundary layers (on average) were discretized with 25 grid points. The dimensions of the O-grids were arrived at based on the value of y^+ and the number of points within the boundary layer, while the dimensions of the H-grids were determined by performing wake convection simulations in the absence of airfoils.

RESULTS

The results reported in this section are for the $1\frac{1}{2}$-stage compressor described above. These results were computed for an inlet (design-flow) Mach number of 0.374, an inlet flow angle of 35 degrees (measured from the axial direction) and an inlet unit Reynolds number of 118,110 per cm (based on the rotor axial chord). The ratio of the stage-exit static pressure to the inlet total pressure was set equal to $P_4/P_{t1} = 1.0663$. The rotation speed of the compressor is 8360 RPM. The free stream turbulence level in the $k-\epsilon$ simulations was set at 3%. The value of the free stream turbulent viscosity (used in place of a dissipation length scale) was set at 10 times the laminar viscosity, based on previous compressor simulations. Stream-tube contraction terms were modelled to approximate three-dimensional effects.

All computations were performed using 2 sub-iterations per time-step and 3000 time-steps per cycle. Here, a cycle is defined as the time it takes a rotor to travel a distance equal to $2\pi rn/N$, where r is the radius at midspan, n is the number of rotor blades being modelled and N is the number of rotor blades in the actual machine. Each simulation was run in excess of 50 cycles to ensure time-periodicity. All time-averaged quantities were calculated over 10 cycles. The computations were performed on Sun Ultra-2 workstations with two processors and 188MB of memory. Each simulation required approximately 8.5×10^{-5} secs/grid point/iteration computation time.

Efficiency Variations, Wake Effects

One of the potential benefits of airfoil clocking is an increase in stage efficiency. Figure 2 and Table 1 show the predicted variations in compressor efficiency with airfoil clocking using both the B-L and $k-\epsilon$ turbulence models. In this investigation, the efficiency is defined as (Oates, 1984)

$$\eta = \frac{\overline{P_t}^{\frac{\gamma-1}{\gamma}} - 1.0}{\overline{T}_t - 1.0} \tag{1}$$

and the average efficiency is calculated using the time-average of the mass-averaged total pressure and total temperature. The two sets of data exhibit efficiency variations on the order of 0.6-0.7%, however the values obtained with the $k-\epsilon$ model are uniformly about 1.5% higher than the B-L values. The differences between the two sets of data are probably due to: 1) the B-L model is solved only on the O-grids while the $k-\epsilon$ equations are solved on the O- and H-grids, leading to more accurate wake definition, and 2) the fact that the B-L model cannot model upstream history or unsteady effects. Although both turbulence models produce qualitatively similar results, all results presented in the remainder of the paper will be based on the $k-\epsilon$ simulations.

Figure 3 and Table 2 show the predicted relative losses in each blade row where the loss is defined as:

$$\omega = \frac{Pt_{in} - Pt_{out}}{Pt_{in}} \tag{2}$$

The highest losses are observed in the rotor passage, while the lowest losses are observed in the first-stage stator passage. The losses in the second-stage stator passage appear to vary the most as the airfoils are clocked. In general, the highest losses occur near the lowest efficiency condition, and the lowest losses occur near the highest efficiency condition.

Figures 4 and 5 illustrate instantaneous entropy contours at the clocking locations corresponding to the lowest and highest efficiencies, respectively. The most notable difference between the two figures is that the wakes in the second-stage stator passage are more diffuse and unsteady at the higher efficiency condition. Both figures illustrate that the combination of wakes from the first-stage stator and rotor lead to a highly disturbed flow field in the second-stage stator passage. Figures 6 and 7 contain the time-averaged entropy contours in the second-stage stator passage for the lowest and highest efficiencies. In these figures, the contours corresponding to the wake of the first stage stator are labelled. Similar to the results of previous compressor studies (*e.g.*, Gundy and Dorney (1997), Saren *et al.*, 1997), the lowest efficiency is observed when the wakes of the first-stage stator are located in the mid-passage region between second-stage stator airfoils, while the highest efficiency is recorded when the wakes of the first-stage stator impact the second-stage stator airfoils (but are slightly offset towards the pressure surface).

It is evident that the location of the first-stage stator wake with respect to the second-stage stator has an impact on the performance of the compressor; what is not clear is if the wake effects are a steady phenomenon, an unsteady phenomenon or a combination of both. In an effort to resolve this question a series of cascade simulations were performed for the second-stage stator. A steady wake with a 5% axial velocity deficit and Gaussian profile was introduced at different (clocking) locations along the inlet to the cascade. Therefore, there was a small angle of attack variation through the wake. The static pressure was constant through the wake. Figure 8 and Table 3 show the variations of the cascade losses as the location of the wake was changed. The (qualitative) variation of the losses was similar to that observed in the unsteady stage simulations; the lowest losses occurred when the wake impacted the airfoils and the highest losses corresponded to the wake residing in the mid-passage region between airfoils. The overall level of the loss variations, however, is much lower in the steady simulations. Thus, the losses in the second-stage stator are only partially due to the angle of attack variations in the wake.

Downloaded from http://asmedigitalcollection.asme.org/GT/proceedings-pdf/GT1998/78620/V001T01A024/2410237/v001t01a024-98-gt-082.pdf by guest on 16 August 2022

Pressure Field Effects

The second contribution to the performance variations is due to changes in the unsteady pressure field. The following discussion is meant to highlight the differences in the unsteady pressure fields and highlight the need for unsteady analyses in compressor design systems.

Figures 9 and 10 contain the time-averaged pressure distributions on the rotor and second-stage stator airfoils, respectively. The distributions are similar at both the lowest and highest efficiencies, except for slightly more loading near the leading edge of the second-stage stator at the highest efficiency conditions. The unsteady pressure amplitude coefficient distributions (which indicate levels of unsteadiness) for the rotor and second-stage stator are presented in Figs. 11 and 12, respectively. The pressure amplitude coefficient is defined as

$$C_p = \frac{P_{max} - P_{min}}{\frac{1}{2}\rho_1 U_m^2} \tag{3}$$

where P_{min} refers to the minimum pressure recorded during 10 blade-passing cycles and P_{max} refers to the maximum pressure recorded during 10 cycles. Along the suction surface of the rotor the pressure unsteadiness is greater at the highest efficiency conditions. On the pressure surface of the rotor the pressure amplitude coefficient corresponding the highest efficiency is greater over the fore part of the airfoil and lower over the aft portion. Along the suction surface of the second-stage stator the pressure unsteadiness is greater at the highest efficiency, while on the pressure surface the unsteadiness is similar for both conditions.

While the pressure amplitude coefficient is a useful method for measuring overall levels of unsteadiness, pressure histories and Fourier decompositions are well-suited for tracing the sources of the unsteadiness. Figure 13 displays the pressure history (over 3 blade-passing cycles) at 25% of the axial chord on the rotor pressure surface, while Fig. 14 illustrates the Fourier decomposition of the trace. These figures show that the unsteadiness is similar for both clocking positions, with the highest efficiency location showing more high-frequency content. At 75% of the axial chord on the pressure surface the unsteadiness is greater at the lowest efficiency conditions (see Figs. 15 and 16); however, the highest efficiency clocking location again displays more high-frequency content. The pressure history and Fourier decomposition for the tap at 1.3% of the axial chord on the second-stage stator suction surface are shown in Figs. 17 and 18, respectively. At this location much more unsteadiness is observed at the highest efficiency conditions. In addition, the magnitude of the second harmonic of the unsteady pressure is much larger than the first harmonic (see Fig. 18). Moving aft to 15% of the suction-surface axial chord (see Figs. 19 and 20), the highest efficiency conditions still exhibit more unsteadiness and frequency content. It is conjectured that at the higher efficiencies the position of the second-stage stator elicits high-frequency unsteadiness; this may be due to pressure responses as the first-stage stator wakes (vorticity) impact the second-stage stator. This also implies that the first-stage stator wakes not only cause steady-state variations in the performance, they induce unsteady variations via the pressure field.

Viscous and Turbulence Effects

The relative location of the first-stage stator wake in the second-stage stator passage can also have an impact on the viscous quantities. Figure 21 shows the time-averaged momentum thickness on the second-stage stator. The momentum thickness is generally greater at the highest efficiency operating conditions, which is consistent with the first-stage stator wakes impacting the second-stage stator airfoils. Both clocking positions show a large increase in the momentum thickness near the leading edge of the suction surface of the airfoil, followed by a rapid decrease and gradual increase over the mid and aft portions of the airfoil, respectively. The time-averaged skin friction coefficients on the second-stage stator are presented in Fig. 22. Similar to previous studies (Dorney and Sharma, 1996; Saren *et al.*, 1997), the current results indicate increases in the skin friction at the highest efficiency conditions.

Instantaneous turbulence intensity contours corresponding to the highest efficiency conditions are shown in Fig. 23. The greatest turbulence intensities are observed in the airfoil wakes, reaching nearly 15%. Moving downstream the flow exhibits increasing large variations of the turbulence intensity in both the streamwise and pitchwise directions. Figure 24 and Table 4 contain the streamwise variations in the time- and pitchwise-averaged turbulence intensities for both the lowest and highest efficiency conditions. In the first-stage stator and rotor passages the average values of the turbulence intensity develop at similar rates. In the second-stage stator passage, however, the turbulence intensity shows larger increases at the highest efficiency conditions ($\approx$0.5%). These results may be used to provide guidance for steady multi-stage flow analyses, in which the level of the turbulence intensity at the inlet of each blade row is often set in an arbitrary manner.

SUMMARY

A quasi three-dimensional unsteady Navier-Stokes analysis has been used to investigate stator clocking in a multistage compressor. The following observations have been made based on the predicted results.

- Stator clocking can result in efficiency gains (or losses) of 0.6-0.7%, which is consistent with previous investigations for low-speed compressors.
- The highest efficiencies are observed when the wake of the first-stage stator impacts the pressure surface of the second-stage stator, while the lowest efficiencies are recorded when the first-stage stator wake resides in the mid-passage region between two second-stage stators. The wake effects contain a component that is steady in nature, but they also elicit unsteady pressure responses which have a significant impact on the losses.
- In general, there is more higher frequency unsteadiness generated when the airfoils are clocked to the best efficiency position; especially near the leading edge on the suction side of the second-stage stator.
- The momentum thickness and skin friction are greater on the second-stage stator at the highest efficiency conditions.

Downloaded from http://asmedigitalcollection.asme.org/GT/proceedings-pdf/GT1998/78620/V001T01A024/2410237/v001t01a024-98-gt-082.pdf by guest on 16 August 2022

- The turbulence intensity decreases in the first-stage stator, then rapidly increases in the rotor and second-stage stator passages. The average values of the turbulence intensity develop at similar rates in the first-stage stator and rotor at all the clocking positions; however, it increases to greater values in the second-stage stator passage at the highest efficiency conditions.

BIBLIOGRAPHY

Baldwin, B. S., and Lomax, H., 1978, "Thin Layer Approximation and Algebraic Model for Separated Turbulent Flow", AIAA Paper 78-257, Huntsville, AL, January.

Barankiewicz, W. S., and Hathaway, M. D., 1997, "Effects of Stator Indexing on Performance in a Low Speed Multistage Axial Compressor," ASME Paper 97-GT-496, Orlando, FL, June.

Capece, V. R., 1987, "Forced Response Unsteady Aerodynamics in a Multistage Compressor", Ph.D. Thesis, Purdue University.

Chien, K.-Y., 1982, "Predictions of Channel and Boundary-Layer Flows with a Low-Reynolds-Number Turbulence Model," *AIAA Journal*, Vol. 20, January, pp. 33-38.

Dorney, D. J., and Verdon, J. M., 1994, "Numerical Simulations of Unsteady Cascade Flow," *ASME Journal of Turbomachinery*, Vol. 116, No. 4, October, pp. 665-675.

Dorney, D. J., and Sharma, O. P., 1996, "A Study of Turbine Performance Increases Through Airfoil Clocking", AIAA Paper 96-2816, Lake Buena Vista, FL, July.

Griffin, L. W., Huber, F. W., and Sharma, O. P., 1995, "Performance Improvement Through Indexing of Turbine Airfoils: Part II - Numerical Simulation," ASME Paper 95-GT-28, Houston, TX, June, also to appear in the *ASME Journal of Turbomachinery*.

Gundy-Burlet, K. L., and Dorney, D. J., 1997a, "Physics of Airfoil Clocking in Axial Compressors," ASME Paper 97-GT-444, Orlando, FL, June.

Gundy-Burlet, K. L., and Dorney, D. J., 1997b, "Investigation of Airfoil Clocking and Inter-Blade Row Gaps in Axial Compressors," AIAA 97-3008, Seattle, WA, July.

Hsu, S. T., and Wo, A. M., 1997, "Reduction of Unsteady Blade Loading by Beneficial Use of Vortical and Potential Disturbances in an Axial Compressor with Rotor Clocking," ASME Paper 97-GT-86, Orlando, FL, June, also to appear in the *ASME Journal of Turbomachinery*.

Huber, F. W., Johnson, P. D., Sharma, O. P., Staubach, J. B., and Gaddis, S. W., 1995, "Performance Improvement Through Indexing of Turbine Airfoils: Part I - Experimental Investigation," ASME Paper 95-GT-27, Houston, TX, June, also to appear in the *ASME Journal of Turbomachinery*.

Oates, G. C., 1984, "Aerothermodynamics of Gas Turbine and Rocket Propulsion", AIAA Educational Series.

Rai, M. M., 1987, "Navier-Stokes Simulations of Rotor/Stator Interactions Using Patched and Overlaid Grids", *AIAA Journal of Propulsion and Power*, Vol. 3, No. 5, Sept., pp.387-396.

Saren, V. E., 1994, "Some Ways of Reducing Unsteady Loads Due to Blade Row Hydrodynamic Interaction in Axial Flow Turbomachines," Second International Conference EAHE, Pilsen, Czech Republic, pp. 160-165.

Saren, V. E., 1995, "Relative Position of Two Rows of an Axial Turbomachine and Effects on the Aerodynamics in a Row Placed Between Them," *Unsteady Aerodynamics and Aeroelasticity of Turbomachines*, Elsevier, pp. 421-425.

Saren, V. E., Savin, N. M., Dorney, D. J., and Zacharias, R. M., 1997, "Experimental and Numerical Investigation of Unsteady Rotor-Stator Interaction on Axial Compressor Stage (with IGV) Performance," 8th International Symposium on Unsteady Aerodynamics and Aeroelasticity of Turbomachines, Stockholm, Sweden, September 14-18.

Towne, C. E., Schwab, J. R., and Bui, T. T., 1993, "Proteus Two-Dimensional Navier-Stokes Computer Code - Version 2.0; Volume 1 - Analysis Description," NASA TM 106336, October.

Walker, G. J., Hughes, J. D., Kohler, I., and Solomon, W. J., 1997, "The Influence of Wake-Wake Interactions on Loss Fluctuations of a Downstream Axial Compressor Blade Row," ASME Paper 97-GT-469, Orlando, FL.

Position, %pitch	η, B-L.	η, $k-\epsilon$
0.0	0.8994	0.9145
12.5	0.9013	0.9162
25.0	0.8999	0.9114
37.5	0.8957	0.9083
50.0	0.8950	0.9087
62.5	0.8948	0.9094
75.0	0.8945	0.9109
87.5	0.8949	0.9140
100.0	0.8994	0.9145

Table 1: Compressor efficiency.

Position	ω-S1	ω-R1	ω-S2
0.0	0.00323	0.01114	0.00557
12.5	0.00318	0.01139	0.00607
25.0	0.00284	0.01207	0.00692
37.5	0.00288	0.01221	0.00742
50.0	0.00289	0.01242	0.00818
62.5	0.00289	0.01332	0.00785
75.0	0.00287	0.01310	0.00718
87.5	0.00313	0.01216	0.00660
100.0	0.00323	0.01114	0.00557

Table 2: Compressor losses.

Downloaded from http://asmedigitalcollection.asme.org/GT/proceedings-pdf/GT1998/78620/V001T01A024/2410237/v001t01a024-98-gt-082.pdf by guest on 16 August 2022

Position, %pitch	ω, B-L
0.0	0.00268
25.0	0.00278
50.0	0.00286
75.0	0.00283
100.0	0.00268

Table 3: Cascade losses.

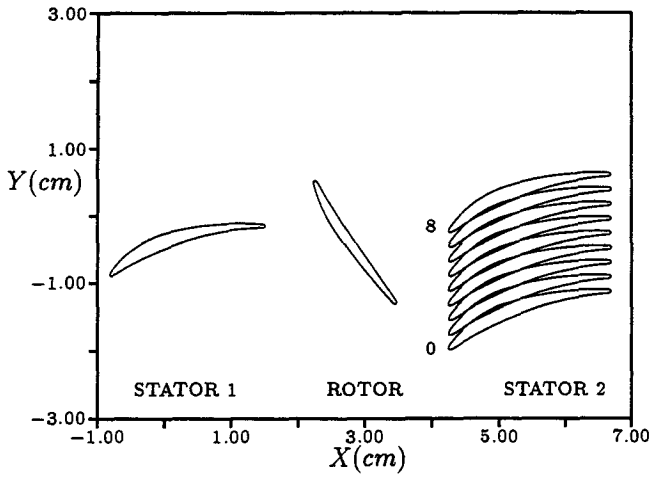

Figure 1: Stage geometry and airfoil clocking positions.

Position	Tu(%) Low η	Tu(%) High η
Inlet	2.928	2.932
Midgap S1-R	2.030	2.021
Midgap R-S2	3.996	3.925
Exit	6.887	7.271

Table 4: Average turbulence.

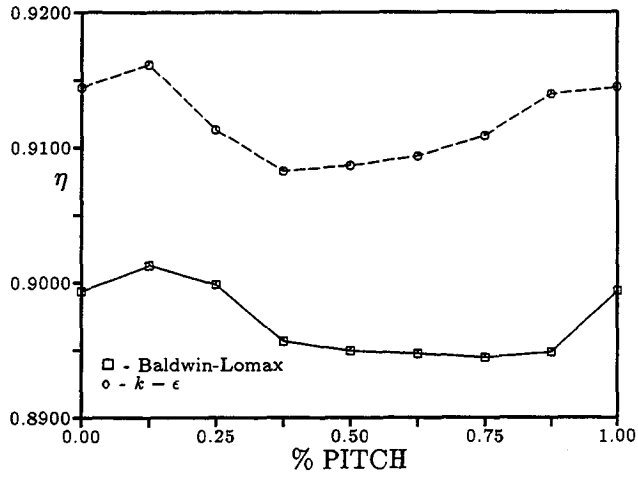

Figure 2: Efficiency vs clocking position.

Downloaded from http://asmedigitalcollection.asme.org/GT/proceedings-pdf/GT1998/78620/V001T01A024/2410237/v001t01a024-98-gt-082.pdf by guest on 16 August 2022

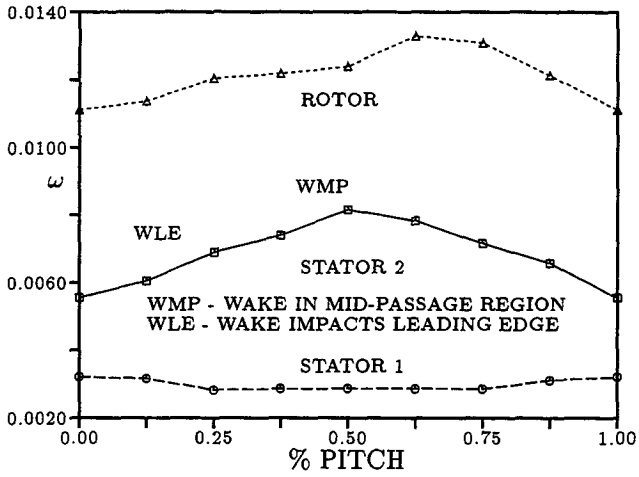

Figure 3: Loss vs clocking position.

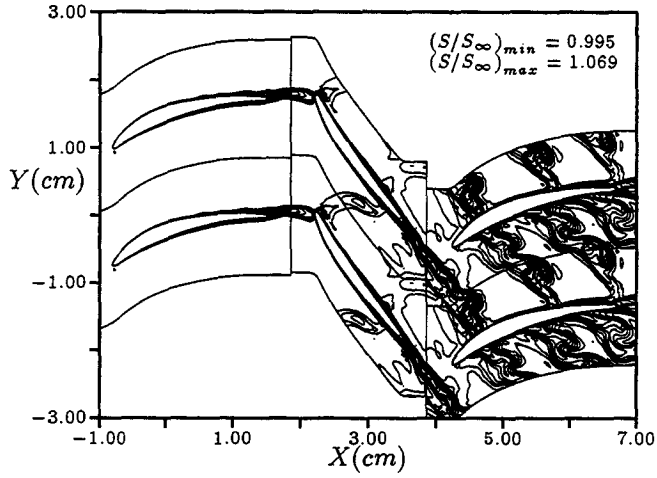

Figure 5: Instantaneous entropy contours - highest η.

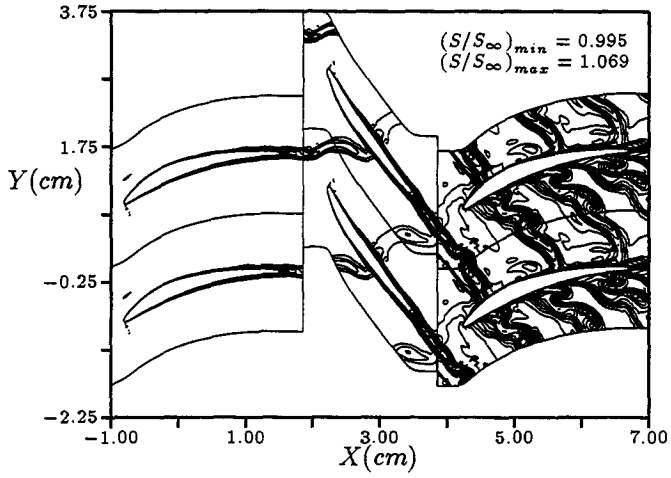

Figure 4: Instantaneous entropy contours - lowest η.

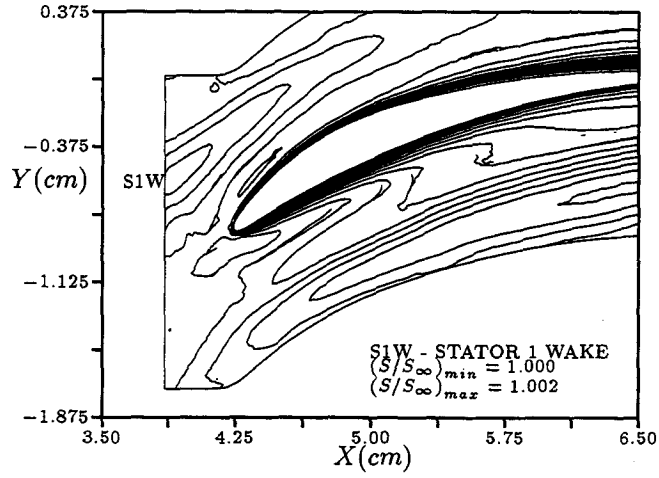

Figure 6: Time-averaged entropy contours in the second-stage stator - lowest η.

Downloaded from http://asmedigitalcollection.asme.org/GT/proceedings-pdf/GT1998/78620/V001T01A024/2410237/v001t01a024-98-gt-082.pdf by guest on 16 August 2022

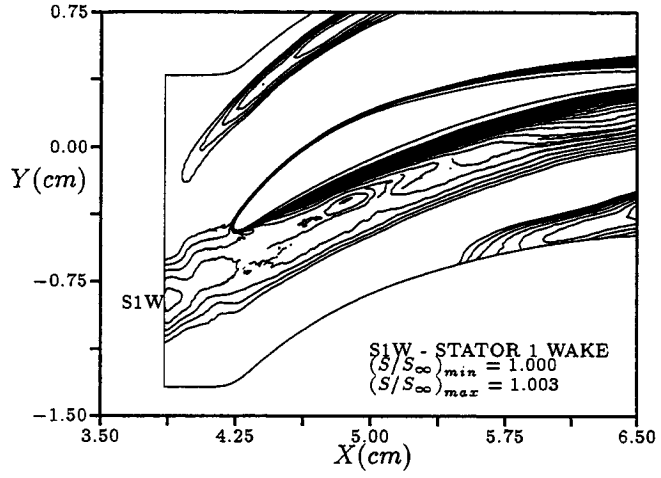

Figure 7: Time-averaged entropy contours in the second-stage stator - highest η.

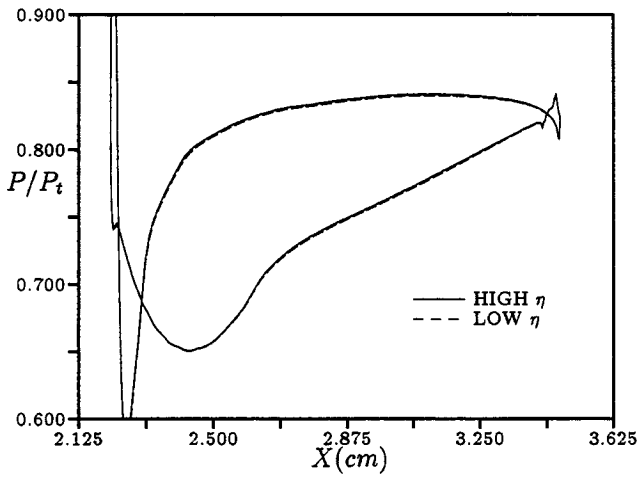

Figure 9: Time-averaged pressure distribution on the rotor.

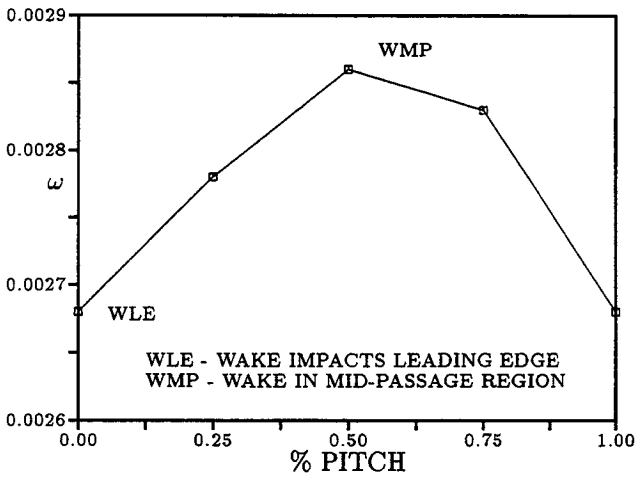

Figure 8: Loss variation due to clocking of a wake in a steady cascade simulation.

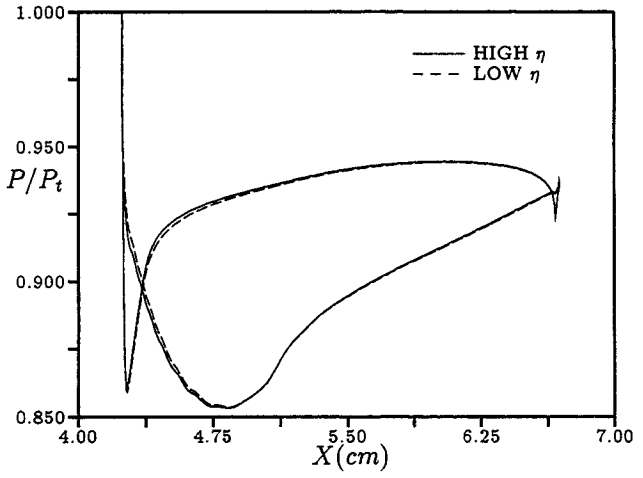

Figure 10: Time-averaged pressure distribution on the second-stage stator.

Downloaded from http://asmedigitalcollection.asme.org/GT/proceedings-pdf/GT1998/78620/V001T01A024/2410237/v001t01a024-98-gt-082.pdf by guest on 16 August 2022

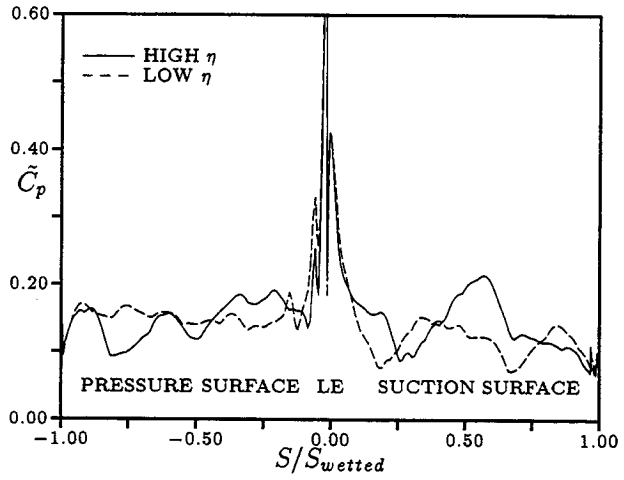

Figure 11: Pressure amplitude coefficient distribution on the rotor.

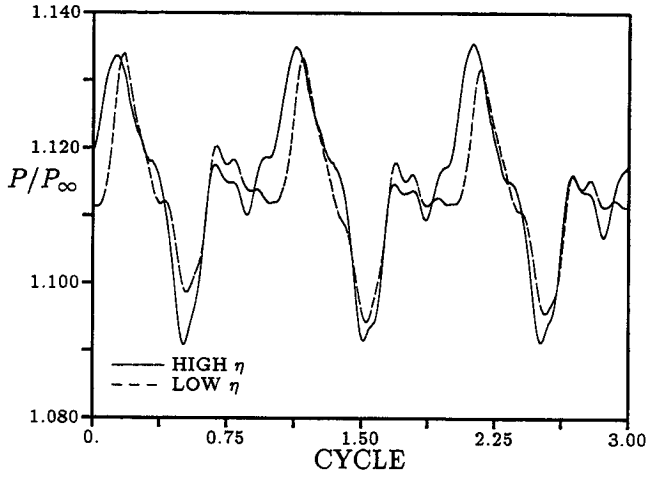

Figure 13: Unsteady pressure history at 25% axial chord on the rotor pressure surface.

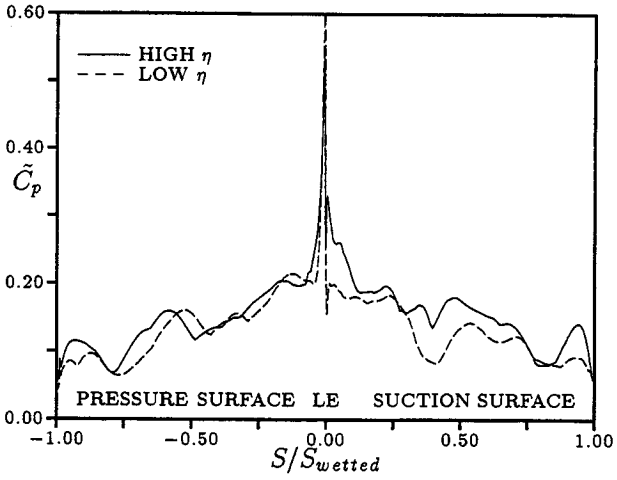

Figure 12: Pressure amplitude coefficient distribution on the second-stage stator.

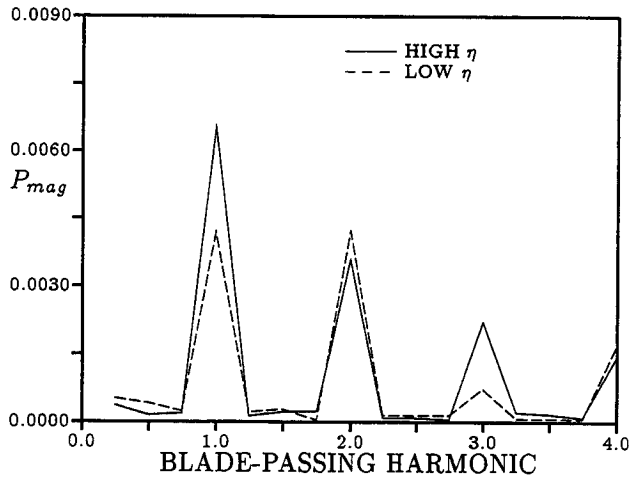

Figure 14: Fourier decomposition of the unsteady pressure at 25% axial chord on the rotor pressure surface.

Downloaded from http://asmedigitalcollection.asme.org/GT/proceedings-pdf/GT1998/78620/V001T01A024/2410237/v001t01a024-98-gt-082.pdf by guest on 16 August 2022

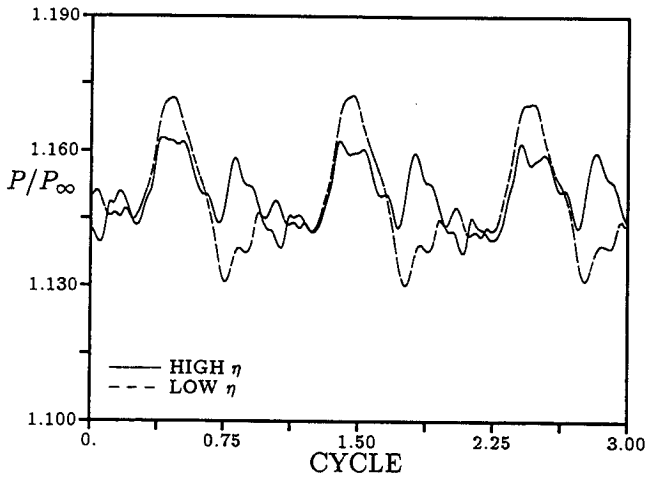

Figure 15: Unsteady pressure history at 75% axial chord on the rotor pressure surface.

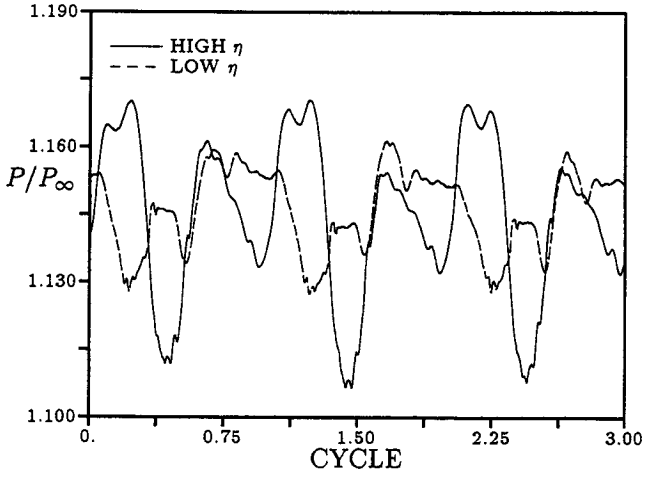

Figure 17: Unsteady pressure history at 1.3% axial chord on the second-stage stator suction surface.

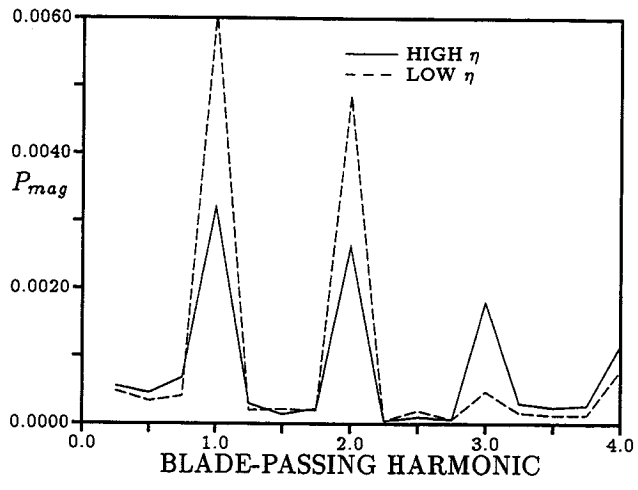

Figure 16: Fourier decomposition of the unsteady pressure at 75% axial chord on the rotor pressure surface.

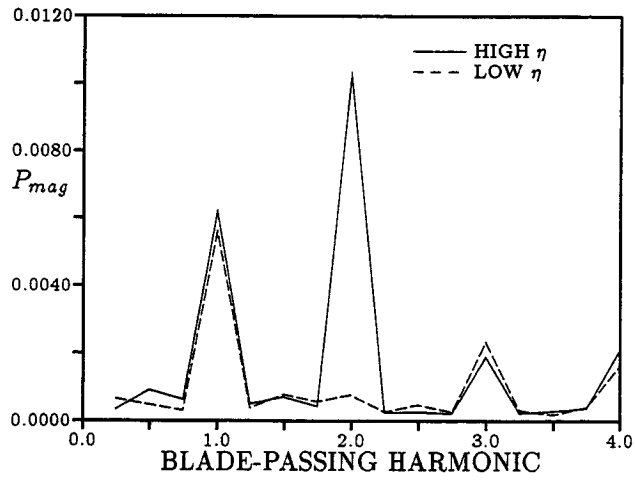

Figure 18: Fourier decomposition of the pressure at 1.3% axial chord on the second-stator suction surface.

Downloaded from http://asmedigitalcollection.asme.org/GT/proceedings-pdf/GT1998/78620/V001T01A024/2410237/v001t01a024-98-gt-082.pdf by guest on 16 August 2022

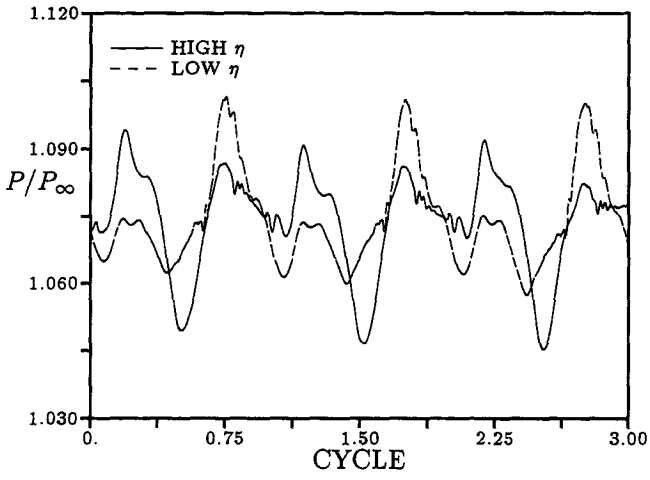

Figure 19: Unsteady pressure history at 15% axial chord on the second-stage stator suction surface.

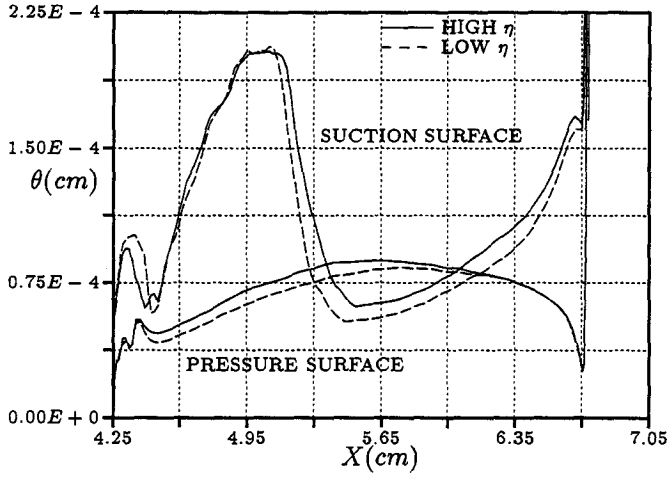

Figure 21: Time-averaged momentum thickness on the second-stage stator.

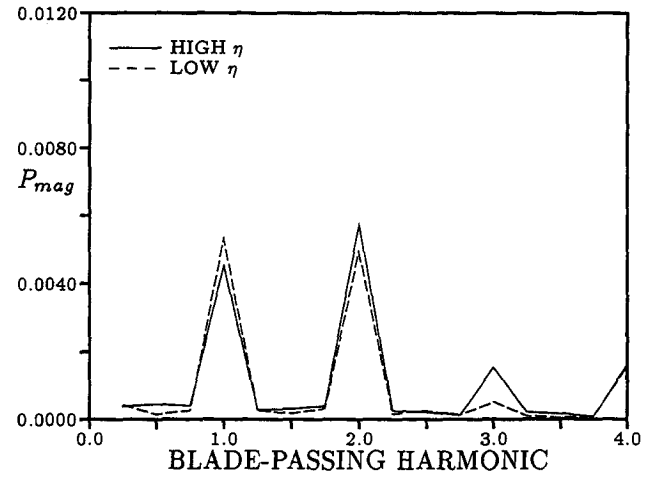

Figure 20: Fourier decomposition of the pressure at 15% axial chord on the second-stator suction surface.

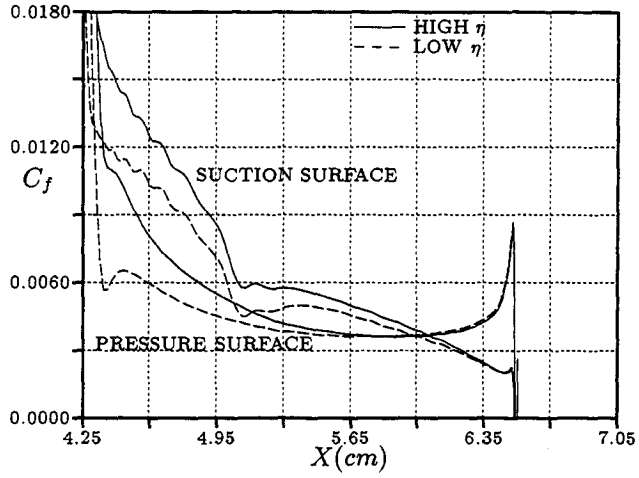

Figure 22: Time-averaged skin friction coefficient on the second-stage stator.

Downloaded from http://asmedigitalcollection.asme.org/GT/proceedings-pdf/GT1998/78620/V001T01A024/2410237/v001t01a024-98-gt-082.pdf by guest on 16 August 2022

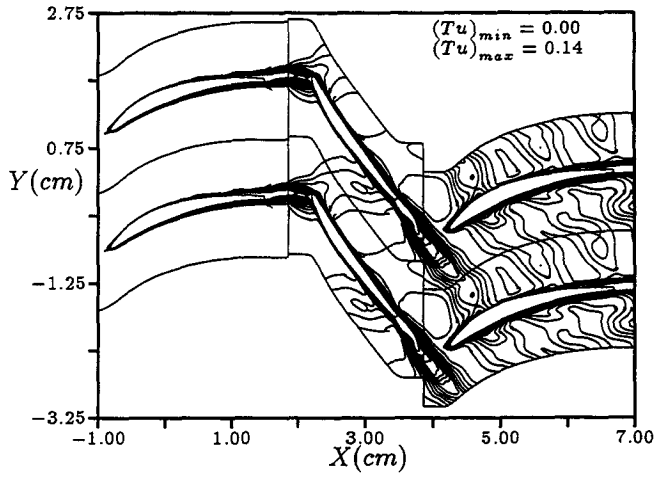

Figure 23: Instantaneous turbulence intensity contours - highest η.

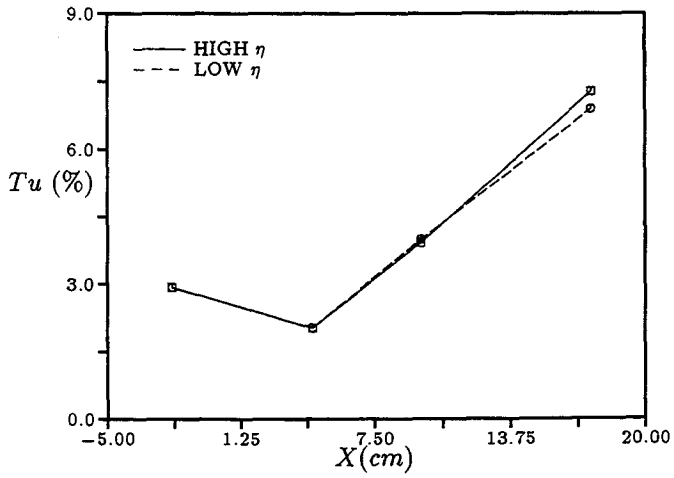

Figure 24: Development of time-averaged turbulence intensity.

Downloaded from http://asmedigitalcollection.asme.org/GT/proceedings-pdf/GT1998/78620/V001T01A024/2410237/v001t01a024-98-gt-082.pdf by guest on 16 August 2022